High-Performance Semitransparent and Bifacial Perovskite Solar Cells with MoO$_x$/Ag/WO$_x$ as the Rear Transparent Electrode

Fengxia Liang, Zhiqin Ying, Yi Lin, Bao Tu, Zheng Zhang, Yudong Zhu, Hui Pan, Haifeng Li, Linbao Luo, Oleg Ageev, and Zhubing He*

Semitransparent solar cells play a crucial role in such typical photovoltaic applications as smart windows, transparent chargeable devices, tandem and bifacial devices, and so on. Relying on the commercial conductive transparent oxides as the front electrodes, the development of rear transparent electrode (RTE) is especially essential. Here, an efficient semitransparent perovskite solar cell (PSC) with the softly deposited transparent MoO$_x$/Ag/WO$_x$ (MAW) as the rear electrode is demonstrated. MoO$_x$ enables the continuously grown silver ultrathin film while the high-refractive-index WO$_x$ capping layer can modulate the whole optical interference and enhance the light transmission throughout the device. As a result, depending on the MAW RTE, the semitransparent normal planar PSC owns the optimal conversion efficiency of 15.40% along with 10.17% in the average visible-light transmission (AVT) simultaneously, which claims the best conversion efficiency of the semitransparent PSCs at such considerable AVT. Combining the optical characterizations, the bifacial performance test of the same device also reveals the uneven absorption due to the different optical interference depending on the light direction, as well as the typical parasitic absorption by the functional layers. This paper paves an alternative and promising way to fabricate high-performance semitransparent optoelectronic devices in the future.

To balance both electricity generation and light transmittance, semitransparent solar cells have attracted extensive attention in recent years owing to their great potential in plenty of applications, including building-integrated photovoltaics, smart windows, windshields, foldable curtains, tandem solar cells, and other architectural and fashion elements.[1,2] For the past decade,

metal halide perovskites solar cells (PSC) have obtained significant progress with a conversion efficiency rising from 3.8% to 25.2%.[3,4] That outstanding conversion efficiency affords a large room to modulate the light transmittance for semitransparent devices. Moreover, the flexibility, neutral coloring, pleasing appearance, and low fabrication costs of PSCs enable their huge potential in the application of semitransparent solar cells.[5]

To construct high-performance transparent PSCs with both high conversion efficiency and high transmittance, it needs both front and rear electrode layers in transparency. The instinct responsibility of front transparent electrodes (FTEs) film deposited on the front glass substrates is to allow the transmittance of solar light,[6–10] and is also more easily deposited in contrast to rear transparent electrodes (RTEs) because the latter films have to be deposited on the underlying perovskite absorber layer. Transparent conductive oxides (TCOs) like indium tin oxide (ITO) and fluorine doped tin oxide dominate FTEs in both photovoltaics and optoelectronics fields.[11] Unfortunately, classical TCOs can hardly be employed as RTEs because their depositions generally need high energy or high temperature, which may damage the underlying perovskite and carrier transport layers.[12] A strategy to overcome this problem is to develop alternative RTEs, such

Prof. F. Liang, Z. Ying, Y. Lin, B. Tu, Z. Zhang, Y. Zhu, Prof. Z. He
Department of Materials Science and Engineering
Shenzhen Key Laboratory of Full Spectral Solar Electricity Generation (FSSEG)
Southern University of Science and Technology
No. 1088, Xueyuan Rd., Shenzhen 518055, China
E-mail: hezb@sustc.edu.cn

Prof. F. Liang, Y. Lin
School of Materials Science and Engineering
Anhui Provincial Key Laboratory of Advanced Functional
Materials and Devices
Hefei University of Technology
No. 193, Tunxi Road, Hefei 230009, China

The ORCID identification number(s) for the author(s) of this article can be found under https://doi.org/10.1002/admi.202000591.

Z. Ying, B. Tu, Prof. H. Pan, Prof. H. Li
Institute of Applied Physics and Materials Engineering
University of Macau
Avenida da Universidade
Taipa 999078, China

Prof. L. Luo
School of Electronic Science and Applied Physics
Hefei University of Technology
No. 193, Tunxi Road, Hefei 230009, China

Prof. O. Ageev
Institute of Nanotechnologies
Electronics and Equipment Engineering
Southern Federal University
2 Shevchenko, Taganrog 347928, Russia

**ADVANCED
SCIENCE NEWS**
www.advancedsciencenews.com

**ADVANCED
MATERIALS
INTERFACES**
www.advmatinterfaces.de

as oxide–metal–oxide (OMO),[9,13] metal mesh,[14] thin metal film,[15–17] metal nanowire,[18,19] conductive polymer,[20] graphene,[6] and carbon nanotube.[8,21] Among these emerging TEs, OMO shows high potential because of its low electrical resistance, good optical transmittance, good mechanical flexibility, cost-effective and mature fabrication process.[22] The first semitransparent PSC with an $MoO_3/Au/MoO_3$ top electrode was reported by Cheng et al. in 2015, resulting in the semitransparent PSC with an average visible-light transmittance (AVT) of 31% and a relatively low conversion efficiency of 5.3%.[13] Yang et al. adopted an $MoO_3/Au/Ag/MoO_3$ top electrode in semitransparent PSCs that were combined in a copper indium gallium selenide tandem device.[23] Pignataro et al. applied an $MoO_x/Au/Cu/MoO_x$ OMO RTE to construct semitransparent PSCs, obtaining device conversion efficiencies of 3.1–12.5% with the corresponding AVT of 24–5%.[24] Zhao et al. demonstrated semitransparent PSCs based on an $SnO_x/Ag/SnO_x$ TE shows an AVT of 29% and a conversion efficiency of above 11%.[22] However, the conversion efficiency of semitransparent PSCs is still low and falls behind in a large gap the corresponding opaque ones. More efforts need to be dedicated to improve its conversion efficiency at some required AVT by modulating RTEs.

In this work, a typical combination of $MoO_x/Ag/WO_x$ (MAW) was successfully introduced as the effective OMO-based RTE to realize high-performance semitransparent PSCs in a device configuration of "Glass/ITO/SnO_2/Perovskite Spiro-OMeTAD/ MAW." Depending on both simulation and experimental optimization, the optimal combination was determined as MoO_x (30 nm)-Ag (12 nm)-MoO_x (30 nm), owning a transmittance of 82.33% at the typical wavelength of 550 nm and a sheet resistance of 10.3 Ω/□. MoO_x is found to be an effective buffer layer by offering the continuous growth of ultrathin Ag film while the WO_x capping layer can remarkably enhance the transmittance by the refractive-index matching at the interface between

MAW and air. Basing on the MAW, the semitransparent PSC shows the best conversion efficiency of 15.40% simultaneously with an AVT of 10.17%, which are outstanding among the recent reports. More optical characterizations are conducted to discover the mechanisms behind it.

To fabricate the MAW semitransparent RTEs, the MoO_x, Ag, and WO_x layers were e-beam evaporated on substrates in sequence (the details are included in the Experimental Section in Supporting Information). The thickness of the Ag interfacial layer should be reduced as thin as possible to allow sufficient light to pass through, while it needs to be thick enough to maintain sufficient conductivity to collect photon-generated carriers. So the silver film thickness can balance the conductivity and transmittance simultaneously to support the growth of homogeneous and continuous ultrathin Ag film by suppressing the 3D island growth mode of Ag on heterogeneous surface.[25] As presented in **Figure 1**a, $R_□$ of the bare Ag and MoO_x/Ag is decreased with increasing Ag thickness. Compared to the 12 nm thick bare Ag electrode with $R_□$ up to 47.8 Ω/□, the MoO_x/Ag (12 nm) electrode exhibits a sharply decreased $R_□$ of 8.6 Ω/□, revealing that the MoO_x buffer layer can greatly affect the film structure and hence the electrical property of the ultrathin Ag. That is because MoO_x can offer a good substrate to form a continuous thin film owing to suitable surface energy and hence enhance good conductivity of silver films grown on it.[26] Moreover, MoO_x has large work function and deep VBM, which facilitate holes transport in devices owing to well matching the band level of the perovskite absorber layer.[9] It is well known that the capping of a transparent high-refractive-index oxide layer on the thin Ag film with a low refractive index can shift the phase of the incident light at their interfaces and then induce destructive interference that reduces the reflection of the Ag film, leading to an increase in the transmittance of the derived stack.[27] Here we usedWO_x as the capping layer
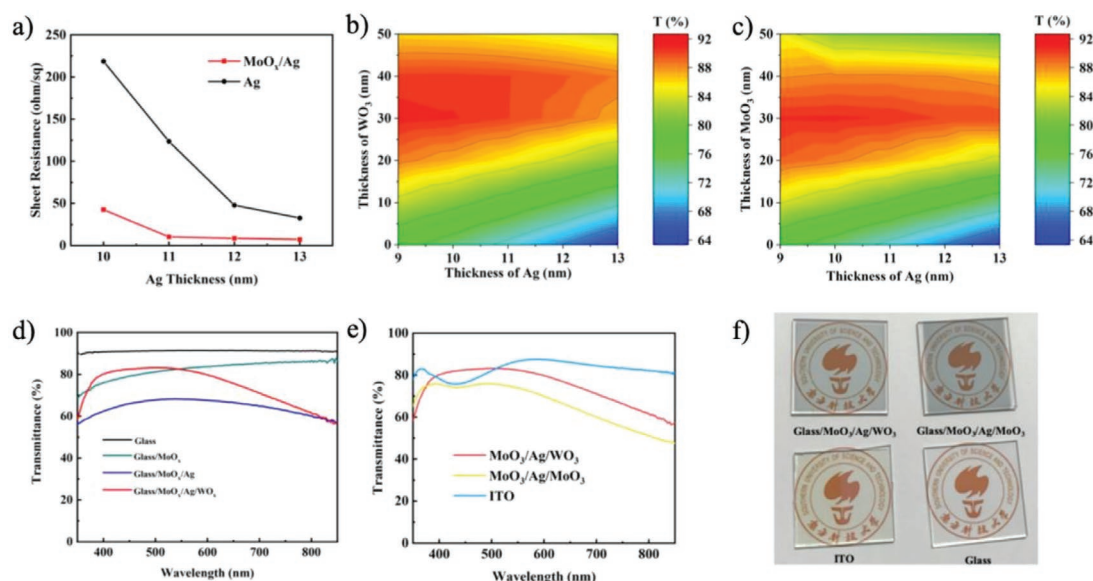
Figure 1. a) Thickness-dependent sheet resistance ($R_□$) of silver films deposited on glass and MoO_x/glass. b) Simulated contour plot of the transmittance at wavelength of 550 nm of b) MoO_x (30 nm)-Ag (x nm)-WO_x (y nm) and c) MoO_x (y nm)-Ag (x nm)-MoO_x (30 nm). d) Optical transmittance spectra of each stack composed of Ag (12 nm), MoO_x (30nm) and WO_x (30 nm) in a range from 350 nm to 850 nm. e) Optical transmittance spectra and f) photographs of MoO_x (30 nm)-Ag (12 nm)-WO_x (30 nm), MoO_x (30 nm)-Ag (12 nm)-MoO_x (30 nm), and the commercial ITO films on glass substrates.

owing to its wide bandgap and visible-light transparency. In addition, WO_x is also chemically stable, water insoluble, and environmentally friendly, which benefits the stability of the electrode as well as the underlying device.[28]

According to our former understanding and experience,[9] the thickness of Ag layer is fixed at 12 nm which is thin enough to allow the light transmission but thick enough to be sufficiently conductive. Figure S1, Supporting Information shows the simulated contour plot of the transmission spectra of MAW with the thickness of Ag film fixed at 12 nm. The optimal transmittance of MAW turns up when thicknesses of MoO_x and WO_x are around 30 nm. Although around the MoO_x thickness of 15 nm, the transmittance also shows considerable values, a threshold thickness is necessary to form continuous and compact film covering a certain area. On the other hand, in common sense, thicker film leads to more compact film, increased crystallinity, and higher conductivity, which promotes effective transportation of electrons or holes in metal oxides. In order to further discriminate the optical matching between each component, the transmittance simulation modulated from the thickness variation between Ag and WO_x (Figure 1b) and between Ag and WO_x (Figure 1c) were conducted. They indicated that the optimized thicknesses of the bottom MoO_x and top WO_x layers are both 30 nm, which is verified by the experimental data shown in Figure S2, Supporting Information. To clarify the transmittance difference and function of each component film in the MAW, the transmittance spectra of all of the films and combinations involved as well as glass used in this work were plotted in Figure 1d. When the blank glass

substrate was coated with MoO_x and Ag successively, the transmittance deteriorates in sequence. Especially, it degrades to a large extent in the red-infrared region. However, after coating the WO_x capping layer, its transmittance rebounds in the visible-light region obviously, which can be ascribed to the matched refractive indexes among each component of glass/MoO_x/Ag/WO_x. To compare the optical images of each combination film, Figure S3, Supporting Information shows optical images of each component film deposited on the blank glass, as well as the bare glass. The transparence difference can be clearly discriminated, and is corresponding to the transmittance spectra shown in Figure 1d. The transmittance spectra of MAW, ITO, and the MoO_x/Ag/MoO_x (MAM) are also shown in Figure 1e. MAW is superior to MAM over the whole wavelength, which is due to the parasitic absorption of MoO_x.[29] After that, MAW is even comparable to ITO, especially in the range from 400 to 500 nm. The peak transmittance of MAW is 83.19% at the wavelength of 498 nm while it is 81.82% for ITO. At the standard point (550 nm), those of MAW and ITO are 82.33% and 86.59%, respectively. Moreover, basing on this combination, the sheet resistance of MAW is as low as 10.3 $\Omega/\square$. That of ITO is also around 10 $\Omega/\square$. The photographs of them deposited on glass along with the pure glass are shown in Figure 1f. The visible transparence of each sample is clearly observed and follows the law of transmittance variation tested in Figure 1e. The comparable optoelectronic properties of MAW and ITO really demonstrate its huge potential utilized in the transparent devices. Hence, the MAW combination was adopted as the RTE for our following solar cells.
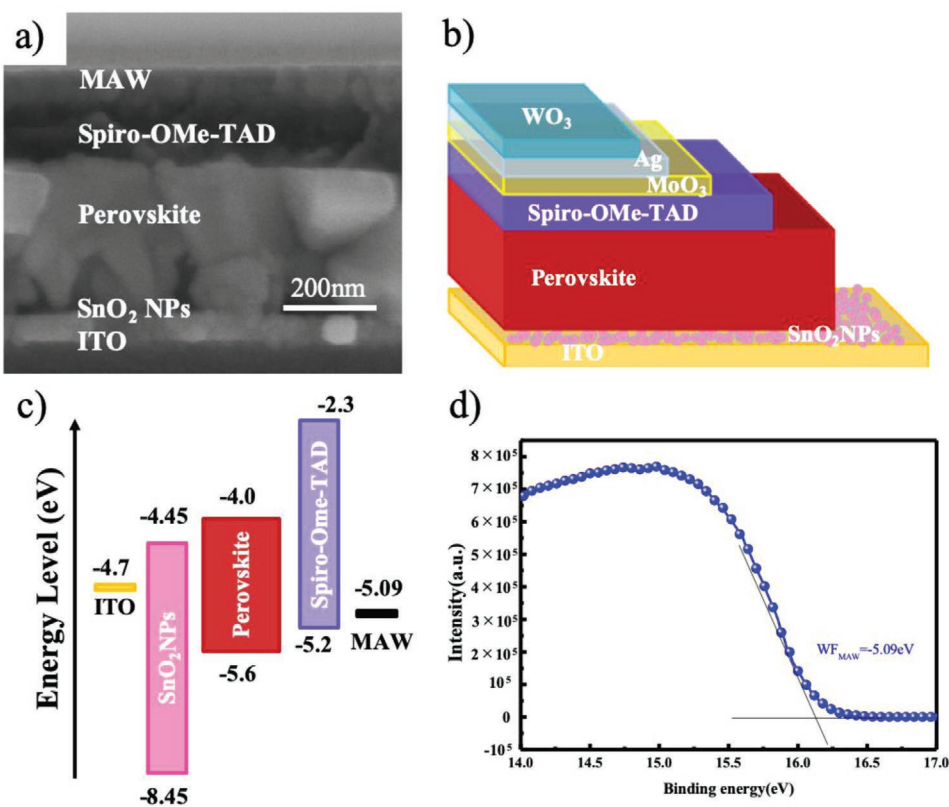
Figure 2. a) Cross-section SEM image of a formal (n-i-p) planar semitransparent PSCs device. b) Device configuration of our semitransparent PSCs. c) Energy level diagram of our devices. d) Ultraviolet photoelectron spectroscopy of the MAW combination.

**ADVANCED
SCIENCE NEWS**
www.advancedsciencenews.com

**ADVANCED
MATERIALS
INTERFACES**
www.advmatinterfaces.de
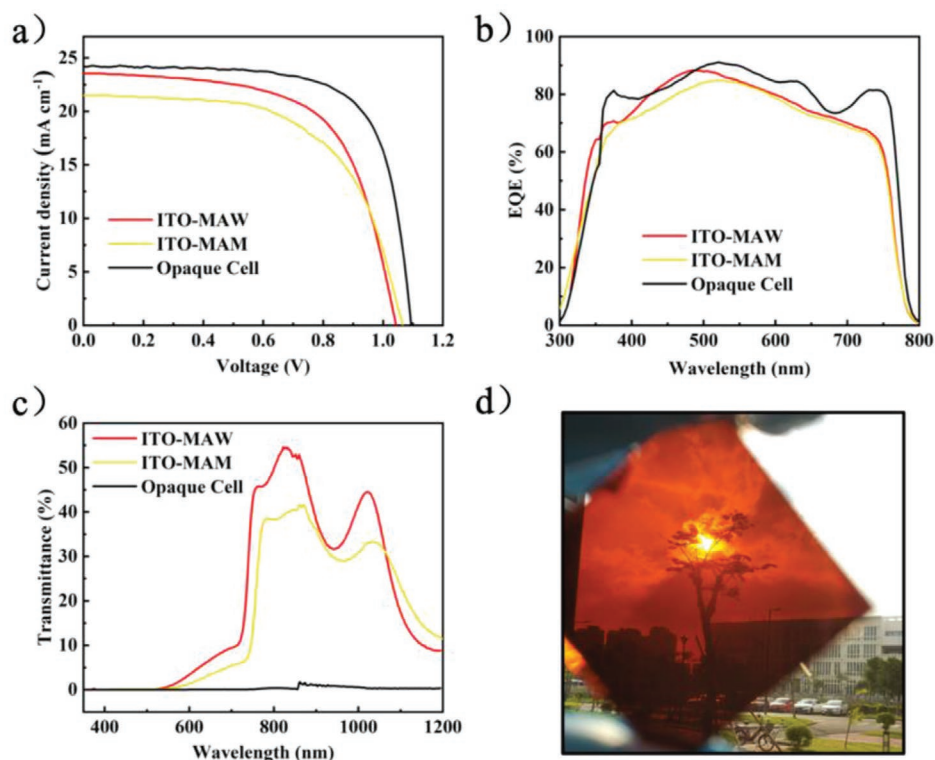
Figure 3. a) J–V characteristics and b) EQE spectra of the semitransparent PSCs with different rear electrodes. c) Optical transmittance of the semitransparent PSCs with different rear electrodes. d) Photograph of a typical semitransparent PSC with MAW as the rear electrode.

Figure 2a shows the cross-section scanning electronic microscopy (SEM) image of our device, where each layer can be discerned. Due to the low resolution of the SEM system we used, the image is not clear enough. To demonstrate its structure more clearly, the schematic configuration is drawn in Figure 2b. The perovskite film is sandwiched by the SnO_2 nanoparticles (SnO_2-NPs) and Spiro-OMeTAD to form an n-i-p normal planar architecture.[30] A continuous and dense layer of SnO_2 NPs film with a thickness of ≈ 30 nm was formed on the ITO glass substrate, acting as electron transport layer (ETL). Then, a 400 nm-thick CsFAMA perovskite was deposited on the surface of the SnO_2 film through one-step spin-coating method. A layer of Spiro-OMeTAD with ≈ 150 nm in thickness was subsequently deposited, serving as hole transport layer (HTL). Finally, 71 nm-thick MAW TE was evaporated on the top of the Spiro-OMeTAD layer. We introduced the MoO_x interlayer into the HTL structure because it proves to be an effective HTL in PSCs owing to its wide bandgap, visible-light transparency, and high work function.[31] The energy band diagram of the complete device is sketched in Figure 2c. When Spiro-OMeTAD contact directly with Ag, a large offset (between the work function (WF) of Ag (≈ -4.6 eV) and the HOMO level of Spiro-OMeTAD (≈ -5.2 eV)) would weaken hole transporting at the interface and hence degrade the device performance.[30,32,33] After inserting the MoO_x buffer layer, the WF increases from -4.6 eV for the bare silver to -5.09 eV for the MAW (Figure 2d), shrinking the offset remarkably by the dipole effect at interface between Ag and Spiro-OMeTAD.[34] More than that, MoO_x also blocks the diffusion of Ag atoms through the underlying layer

and causes the reaction with iodine ions, resulting in the degradation of devices. Moreover, compared to other transition metal oxides, MoO_x has the additional advantage of low sublimation point, so that it can be easily evaporated with low temperature, which prevents the underlying Spiro-OMeTAD film from high energy damage.[35]

Basing on the device structure (Figure 2), **Figure 3**a shows J–V curves of the semitransparent solar cells with both MAW and MAM as RTEs for comparison, along with the control device with thick silver as the rear electrode. For the control device (opaque cell), the device exhibited a PCE of 17.30% with a J_{sc} of 23.7 mA cm^{-2}, V_{oc} of 1.02 V and FF of 0.716. For comparison, the routine device with thick gold as the rear electrode was also fabricated and owns a PCE of 18.87% with a J_{sc} of 24.2 mA cm^{-2}, V_{oc} of 1.09 V and FF of 0.713 (Figure S4, Supporting Information), which was comparable to the performance of similar devices reported on other studies.[30] According to the identical process, both device FF values keep almost the same. Whereas, J_{sc} and V_{oc} of the silver-based devices turn obviously lower than those of the gold-based devices, which can be attributed to more mismatched band alignment of silver with shallower work function at the cathode interface. For the MAM-based device (ITO-MAM), its conversion efficiency arrives at 14.2%, with a J_{sc} of 21.50 mA cm^{-2} and a V_{oc} of 1.06 V. For the optimal MAW-based device (ITO-MAW), its conversion efficiency is enhanced to 15.4%, with an increased J_{sc} of 22.8 mA cm^{-2} and a decreased V_{oc} 1.03 V. The photovoltaic parameters of those devices are also summarized in **Table 1**. The external quantum efficiency (EQE) measurements were

Table 1. The photovoltaic performances of the PSCs with different rear electrodes.

	J_{sc} [mA cm^{-2}]	V_{oc} [V]	FF	PCE [%]
ITO-MAW	22.8	1.03	0.660	15.4
ITO-MAM	21.5	1.06	0.624	14.22
Opaque cell	23.7	1.02	0.716	17.30

conducted to verify the improvement of J_{sc} collected by J–V curves in Figure 3a. The statistical data of each device parameter in a batch of 24 PSCs are summarized in Figure S5, Supporting Information. Obviously, by use of RTE, the device performance is obviously inferior to the opaque ones because some amount of light is transmitted and herein lost.[16] In a view of their EQE spectra (Figure 3b), the semitransparent devices exhibit substantially lower photon-to-electron conversion rate, especially at long wavelengths from 500 to 800 nm. That may be attributed to the light loss because the interfacial charge transport has been improved by more suitable WF of MAW. Whereas, the EQE loss around 350 nm may be ascribed to the extinction effect of silver NPs by means of the so-called plasmonic effect.[36] If we compare the response of MAW- and MAM-based devices, they are almost the same except for the difference at the wavelength ranging from 350 to 550 nm, which contributes the J_{sc} difference that occurred in the above J–V curves.

To define the light transmission of the three kinds of devices, the transmittance spectra of the intact devices were characterized by the UV–vis spectroscopy (Figure 3c). The light loss discussed above (from 500 to 800 nm) is examined by those transmittance spectra. As expected, in the control opaque device, the transmittance is almost zero along the wavelength from 300 to 1200 nm while the abrupt increase around 880 nm is due to the exchange of CCD collector in our equipment.

In contrast to the control opaque one, both MAW- and MAM-based devices show remarkable transmittance, especially at the wavelength ranging from 400 to 1200 nm, with an integrated transmission ratio of 21.56% and 17.63%, respectively (Figure 3c). This value for the MAW device is the highest reported one at that wavelength range as far as we know,[37,38] which announces the huge potential for the utilization of infrared lights in an integrated system. The transmittance of the MAW device (red) is higher than that of the MAM one over the whole wavelength. Combining with the EQE spectra difference, it demonstrates that the MAW has higher internal quantum efficiency (IQE) than the MAM, which may be attributed to the better band level

matching and herein lower recombination at the anode interface.[39] Because the absorption edge of our CsFAMA perovskite layer is near 800 nm, we adopt the AVT at the visible-light wavelength ranging from 400 to 800 nm to evaluate the transmittance of the semitransparent devices, subjecting to the general rule in this field.[40] The obtained AVT is 10.17% for the MAW and 6.11% for the MAM, respectively. The visual transmittance can also be examined by the photo taken in a view of solar light transmission (Figure 3d), where we can clearly distinguish sun, the peripheral scenery, and even cloud in the sky.

For the bifacial solar cells, the dual conversion efficiency is also what we concerned.[41] The bifacial J–V characteristics of the MAW-based semitransparent PSCs with the light irradiated at both the ITO and MAW sides were also shown in **Figure 4**a. Illumination from the ITO side showed a higher performance than illumination from the MAW side, mainly because of a higher J_{sc} of 22.8 versus 15.1 mA cm^{-2}. We attributed the lower J_{sc} to the reflection of silver layer along with the parasitic absorption of Spiro-OMeTAD and MoO$_x$ when they stay at the front light-in window[42] (Figure 4a). To further clarify the optical absorption of the typical layers, we also conducted the bifacial reflectance and transmittance spectra of the device (Figure 4b,c). Compared with the ITO glass side, the reflectance spectra illuminated at the MAW side exhibits lower in the two spans in wavelength of 350–475 nm and 500–600 nm (Figure 4b), which is in accordance with the corresponding absorption spectra (Figure 4c). As discussed above, the absorption at the wavelength from 350 to 475 nm can be attributed to Spiro-OMeTAD and MoO$_x$ while the other one can be ascribed to the extinction of thin silver film. The correlated difference in both the reflectance and the absorption spectra at the wavelength from 600 to 900 nm can be ascribed to the difference of optical interference in the device depending on the light-in direction, resulting in the different absorption of incident light by the perovskite active layer.[43] Along with the above two parasitic absorptions, that also examines the J_{sc} difference shown in Figure 4a.

Figure 5 and Table S1, Supporting Information summarize the recently reported relative OMO-based RTEs for the transparent PSCs. Basing on the MAW RTE in this work, our semitransparent device owns an AVT of 10.17% and the conversion efficiency of 15.4%, which is the highest reported value at a considerable AVT as far as we know. That clearly demonstrates the big potential of MAW utilized in semitransparent devices regarding the balance between PCE and AVT.
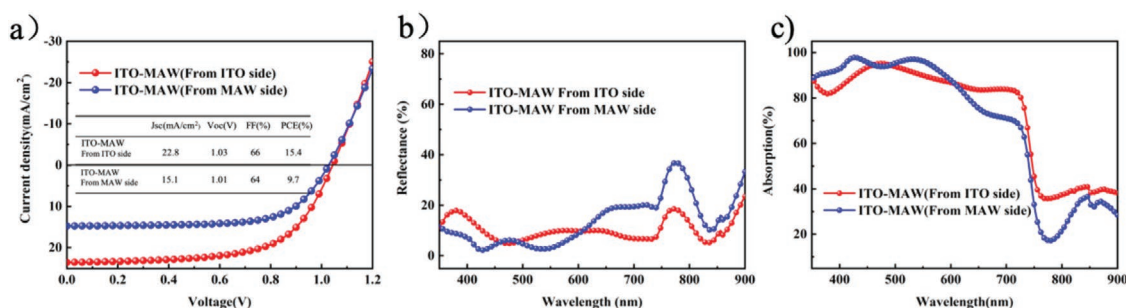
Figure 4. a) J–V characteristics, b) reflection, and c) absorption of semitransparent solar cells with MAW electrode upon illumination via the ITO/MAW electrode.

**ADVANCED
SCIENCE NEWS**
www.advancedsciencenews.com

**ADVANCED
MATERIALS
INTERFACES**
www.advmatinterfaces.de
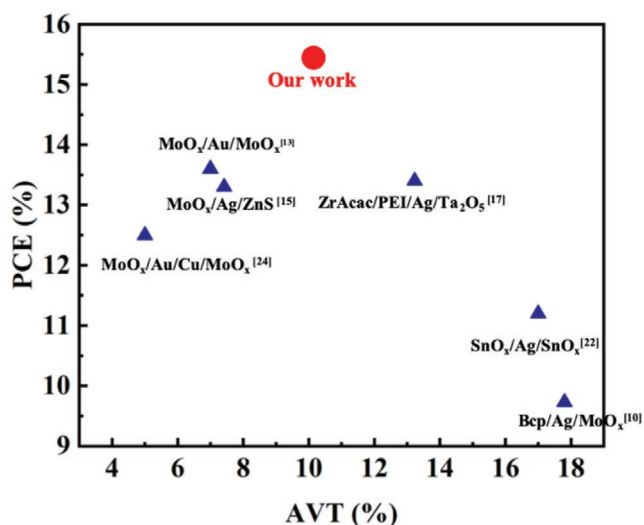
Figure 5. The performances of recently reported semitransparent PSCs based on different RTE combinations, with the MAW-based device of this work included.

In summary, we successfully developed a general combination of MAW as the RTE for constructing the semitransparent PSCs via e-beam evaporation method. Through modulating the thickness of each layer, our optimized MAW owns an optimal transmittance of 83.19% at the wavelength around 550 nm and low sheet resistance of 10.3 $\Omega/\square$, which competes with the commercial ITO. Importantly, the competent MAW can be deposited on the underlying perovskite absorber layer by "soft" evaporation tool other than high energy sputtering. MoO_x affords good substrate to grow continuous silver film while WO_x accounts for the enhancement of light absorption via optical interference. The MAW combination offers more matching work function with Spiro-OMeTAD. Based on that MAW RTE, the semitransparent normal (n-i-p) planar PSC was successfully fabricated and owns the best PCE of 15.40% along with 10.17% in AVT, which claims the best conversion efficiency of the semitransparent PSCs at such considerable AVT. Moreover, combining the optical characterizations, the bifacial performance test of the same device also reveals the parasitic absorption from silver and Spiro-OMeTAD, which especially discovers the uneven absorption by the perovskite active layer due to the different optical interference depending on the light direction. This work definitely paves an alternative and promising way to realize high-performance semitransparent optoelectronic devices by function of the MAW series in the future.

Supporting Information

Supporting Information is available from the Wiley Online Library or from the author.

Acknowledgements

Conflict of Interest

The authors declare no conflict of interest.

Keywords

[1] Y. Li, G. Xu, C. Cui, Y. Li, *Adv. Energy Mater.* **2017**, *8*, 1701791.
[2] D. P. McMeekin, G. Sadoughi, W. Rehman, G. E. Eperon, M. Saliba, M. T. Hörantner, A. Haghighirad, N. Sakai, L. Korte, B. Rech, M. B. Johnston, L. M. Herz, H. J. Snaith, *Science* **2016**, *351*, 151.
[3] A. Kojima, K. Teshima, Y. Shirai, T. Miyasaka, *J. Am. Chem. Soc.* **2009**, *131*, 6050.
[4] National Renewable Energy Laboratory, Best Research-Cell Efficiencies chart, https://www.nrel.gov/pv/ (accessed: December 2019).
[5] S. P. Dunfield, D. T. Moore, T. R. Klein, D. M. Fabian, J. A. Christians, A. G. Dixon, B. Dou, S. Ardo, M. C. Beard, S. E. Shaheen, J. J. Berry, M. F. A. M. van Hest, *ACS Energy Lett.* **2018**, *3*, 1192.
[6] P. You, Z. Liu, Q. Tai, S. Liu, F. Yan, *Adv. Mater.* **2015**, *27*, 3632.
[7] J. H. Heo, H. J. Han, M. Lee, M. Song, D. H. Kim, S. H. Im, *Energy Environ. Sci.* **2015**, *8*, 2922.
[8] S. N. Habisreutinger, R. J. Nicholas, H. J. Snaith, *Adv. Energy Mater.* **2016**, *7*, 1601839.
[9] F. Liang, Y. Lin, Z. He, W. Chen, Y. Zhu, T. Chen, L. Liang, S. Ma, Y. Wu, B. Tu, D. Wang, Z. Zhang, L. Luo, Z. He, *J. Mater. Chem. A* **2018**, *6*, 19330.
[10] G. M. Kim, T. Tatsuma, *Sci. Rep.* **2017**, *7*, 10699.
[11] H. S. Jung, G. S. Han, N.-G. Park, M. J. Ko, *Joule* **2019**, *3*, 1850.
[12] F. Fu, T. Feurer, T. Jäger, E. Avancini, B. Bissig, S. Yoon, S. Buecheler, A. N. Tiwari, *Nat. Commun.* **2015**, *6*, 8932.
[13] E. D. Gaspera, Y. Peng, Q. Hou, L. Spiccia, U. Bach, J. J. Jasieniak, Y.-B. Cheng, *Nano Energy* **2015**, *13*, 249.
[14] D. Bryant, P. Greenwood, J. Troughton, M. Wijdekop, M. Carnie, M. Davies, K. Wojciechowski, H. J. Snaith, T. Watson, D. Worsley, *Adv. Mater.* **2014**, *26*, 7499.
[15] H. Kim, H. S. Kim, J. Ha, N. G. Park, S. Yoo, *Adv. Energy Mater.* **2016**, *6*, 1502466.
[16] Q. Xue, Y. Bai, M. Liu, R. Xia, Z. Hu, Z. Chen, X. F. Jiang, F. Huang, S. Yang, Y. Matsuo, H. L. Yip, Y. Cao, *Adv. Energy Mater.* **2016**, *7*, 1602333.
[17] Z. Ying, W. Chen, Y. Lin, Z. He, T. Chen, Y. Zhu, X. Zhang, X. Yang, A. B. Djurišić, Z. He, *Adv. Opt. Mater.* **2019**, *7*, 1801409.
[18] C.-Y. Chang, K.-T. Lee, W.-K. Huang, H.-Y. Siao, Y.-C. Chang, *Chem. Mater.* **2015**, *27*, 5122.
[19] Y. Fang, Z. Wu, J. Li, F. Jiang, K. Zhang, Y. Zhang, Y. Zhou, J. Zhou, B. Hu, *Adv. Funct. Mater.* **2018**, *28*, 1705409.
[20] K. M. Kim, S. Ahn, W. Jang, S. Park, O. O. Park, D. H. Wang, *Sol. Energy Mater. Sol. Cells* **2018**, *176*, 435.

**ADVANCED
SCIENCE NEWS**

www.advancedsciencenews.com

**ADVANCED
MATERIALS
INTERFACES**

www.advmatinterfaces.de

[21] F. R. Li, Y. Xu, W. Chen, S. H. Xie, J. Y. Li, *J. Mater. Chem. A* **2017**, *5*, 10374.

[22] J. Zhao, K. O. Brinkmann, T. Hu, N. Pourdavoud, T. Becker, T. Gahlmann, R. Heiderhoff, A. Polywka, P. Görrn, Y. Chen, B. Cheng, T. Riedl, *Adv. Energy Mater.* **2017**, *7*, 1602599.

[23] Y. Yang, Q. Chen, Y.-T. Hsieh, T.-B. Song, N. D. Marco, H. Zhou, Y. Yang, *ACS Nano* **2015**, *9*, 7714.

[24] G. Giuliano, S. Cataldo, M. Scopelliti, F. Principato, D. C. Martino, T. Fiore, B. Pignataro, *Adv. Mater. Technol.* **2019**, *4*, 1800688.

[25] J. Zhu, X. Yang, Z. Yang, D. Wang, P. Gao, J. Ye, *Adv. Funct. Mater.* **2018**, *28*, 1705425.

[26] S. Schubert, M. Hermenau, J. Meiss, L. Müller-Meskamp, K. Leo, *Adv. Funct. Mater.* **2012**, *22*, 4993.

[27] H. Kang, S. Jung, S. Jeong, G. Kim, K. Lee, *Nat. Commun.* **2015**, *6*, 6503.

[28] G.-W. Kim, G. Kang, K. Choi, H. Choi, T. Park, *Adv. Energy Mater.* **2018**, *8*, 1801386.

[29] J. Meyer, S. Hamwi, M. Kroger, W. Kowalsky, T. Riedl, A. Kahn, *Adv. Mater.* **2012**, *24*, 5408.

[30] B. Tu, Y. Shao, W. Chen, Y. Wu, X. Li, Y. He, J. Li, F. Liu, Z. Zhang, Y. Lin, X. Lan, L. Xu, X. Shi, A. M. C. Ng, H. Li, L. W. Chung, A. B. Djurišić, Z. He, *Adv. Mater.* **2019**, *31*, 1805944.

[31] T. Brezesinski, J. Wang, S. H. Tolbert, B. Dunn, *Nat. Mater.* **2010**, *9*, 146.

[32] S. Albrecht, M. Saliba, J. P. C. Baena, F. Lang, L. Kegelmann, M. Mews, L. Steier, A. Abate, J. Rappich, L. Korte, R. Schlatmann, M. K. Nazeeruddin, A. Hagfeldt, M. Gratzel, B. Rech, *Energy Environ. Sci.* **2016**, *9*, 81.

[33] W. Chen, Y. Zhou, L. Wang, Y. Wu, B. Tu, B. Yu, F. Liu, H.-W. Tam, G. Wang, B. D. Aleksandra, L. Huang, Z. He, *Adv. Mater.* **2018**, *30*, 1800515.

[34] P. Liu, X. Liu, L. Lyu, H. Xie, H. Zhang, D. Niu, H. Huang, C. Bi, Z. Xiao, J. Huang, Y. Gao, *Appl. Phys. Lett.* **2015**, *106*, 193903.

[35] L. Kranz, A. Abate, T. Feurer, F. Fu, E. Avancini, J. Löckinger, P. Reinhard, S. M. Zakeeruddin, M. Grätzel, S. Buecheler, A. N. Tiwari, *J. Phys. Chem. Lett.* **2015**, *6*, 2676.

[36] P. Wang, D. Zhang, D. H. Kim, Z. Qiu, L. Gao, R.-I. Murakami, X. Song, *J. Appl. Phys.* **2009**, *106*, 103104.

[37] B. Shi, L. Duan, Y. Zhao, J. Luo, X. Zhang, *Adv. Mater.* **2019**, *32*, 1806474.

[38] Q. Xue, R. Xia, C. J. Brabec, H.-L. Yip, *Energy Environ. Sci.* **2018**, *11*, 1688.

[39] D. C. Lim, J. H. Jeong, K. Hong, S. Nho, J.-Y. Lee, Q. V. Hoang, S. K. Lee, K. Pyo, D. Lee, S. Cho, *Prog. Photovoltaics* **2018**, *26*, 188.

[40] C.-C. Chueh, S.-C. Chien, H. L. Yip, J. F. Salinas, C. Z. Li, K. S. Chen, F. C. Chen, W. C. Chen, K. Y. Jen, *Adv. Energy Mater.* **2013**, *3*, 417.

[41] R. Asadpour, R. V. K. Chavali, M. R. Khan, M. A. Alam, *Appl. Phys. Lett.* **2015**, *106*, 243902.

[42] Z. Wang, Z. Song, Y. Yan, S. Liu, D. Yang, *Adv. Sci.* **2019**, *6*, 1801704.

[43] S. Pang, X. Li, H. Dong, D. Chen, W. Zhu, J. Chang, Z. Lin, H. Xi, J. Zhang, C. Zhang, Y. Hao, *ACS Appl. Mater. Interfaces* **2018**, *10*, 12731.